Research article

Ali Ramazani, Farzaneh Shayeganfar, Jaafar Jalilian and Nicholas X. Fang*

# Exciton-plasmon polariton coupling and hot carrier generation in two-dimensional SiB semiconductors: a first-principles study

https://doi.org/10.1515/nanoph-2019-0363
Received September 15, 2019; revised November 27, 2019; accepted December 9, 2019

**Abstract:** Exciton (strong electron–hole interactions) and hot carriers (HCs) assisted by surface plasmon polaritons show promise to enhance the photoresponse of nanoelectronic and optoelectronic devices. In the current research, we develop a computational quantum framework to study the effect of coupled exciton and HCs on the photovoltaic energy distribution, scattering process, polarizability, and light emission of two-dimensional (2D) semiconductors. Using a stable 2D semiconductor (semihydrogenated SiB) as our example, we theoretically show that external strain and thermal effect on the SiB can lead to valley polarized plasmon quasiparticles and HC generation. Our results reveal that the electron–phonon and electron–electron (e–e) interactions characterize the correlation between the decay rate, scattering of excitons, and generation of HCs in 2D semiconductors. Moreover, phonon assisted luminescence spectra of SiB suggest that light emission can be enhanced by increasing strain and temperature. The polarized plasmon with strong coupling of electronic and photonics states in SiB makes it as a promising candidate for light harvesting, plasmonic photocurrent devices, and quantum information.

**Keywords:** surface plasmon; hot carrier; valley polaritons; luminescence; strain engineering.

***Corresponding author: Nicholas X. Fang,** Department of Mechanical Engineering, Massachusetts Institute of Technology, Cambridge, MA, USA, e-mail: nicfang@mit.edu. https://orcid.org/0000-0001-5713-629X
**Ali Ramazani:** Department of Mechanical Engineering, Massachusetts Institute of Technology, Cambridge, MA, USA
**Farzaneh Shayeganfar:** Department of Civil and Environmental Engineering, Rice University, Houston, TX, USA
**Jaafar Jalilian:** Department of Physics, College of Sciences, Yasouj University, Yasouj, Iran

## List of nonstandard abbreviations

| | |
|---|---|
| DFT | Density functional theory |
| HCs | Hot carriers |
| QPs | Quasiparticles |
| SP | Surface plasmon |
| SPP | Surface plasmon polariton |
| H-SiB | Semihydrogenated SiB |
| BSE | Beth–Salpeter Equation |
| MFP | Mean free path |

## 1 Introduction

After the first isolation of two-dimensional (2D) graphene monolayers in 2004 [1, 2], additional novel 2D nanomaterials with similar properties have been sought for a wide range of applications. Recently, new graphene-like materials made by combining groups III–IV elements have become of great interest. For instance, Tománek et al. [3] have investigated structural and electronic properties of 2D boron–carbide monolayers, such as BC, $BC_3$, $BC_5$, and $BC_7$ by utilizing first-principles calculations. Their results demonstrated that those structures possess suitable structural stability and semiconducting characteristics. Due to the outstanding properties of these compounds, many computational and experimental research groups have sought to understand their structure–property relationship for a wide range of applications such as superconductivity [4], electrical devices [5], half-metallicity [6], and hydrogen storage [7]. For instance, the structure and properties of 2D boron–silicon have been predicted computationally using first-principles calculations. For example, Hansson et al. [8] determined that low-dimensional honeycomb SiB nanosheets possess metallic behavior. They found that this compound is of satisfactory structural stability relative to silicene and boron sheets [9–11]. Unlike Hansson et al. [8], who stated that the boron and silicon atoms are distributed alternately in the honeycomb SiB lattice, Dai et al. [12] presented a new stable 2D SiB structure

consisting of uniformly distributed boron dimers and silicon dimers. This new configuration expresses a nonmagnetic metallic behavior for SiB [12]. Ding and Wang [13] showed using first-principles calculations that a 2D SiB monolayer possesses a washboard-like buckled structure, but they did not address its structural stability. Recently, Aizawa et al. [14] reported the fabrication of 2D silicon–boron compounds on the ZrB2(0001) as a good substrate for B or Si adsorption. Their findings suggest that $Si_3B_6$ can reproduce the measured phonon dispersion by using high-resolution electron energy-loss spectroscopy.

Surface plasmon polaritons (SPPs) are the most common type of hybrid modes of photons and excited charge dipole in crystals [15, 16]. Surface plasmon polaritons can be engineered to have photocurrent energy in the desired wavelength and long lifetime [16, 17]. Surface plasmon polariton excitation by photon absorption creates hot carriers (HCs) as any energetic electron or hole through plasmon polariton decay. Photocurrent energy and resonance energy with controlled HCs flow [18] are determined by tuning two factors of size and shape in plasmonic nanomaterials [19]. Ultrafast relaxation of HCs makes capturing of them a difficult premise [20]. To overcome their limitation of short lifetime [20] and maximize the photocurrent efficiency [21, 22], the decay rate and scattering path of hot holes and electrons must be specified [23]. Several experiments can probe this dynamic path directly in metals through time-resolved ultrafast pump probe [24] or indirectly by scanning changes of SP resonances [25]. For following of electro-optic and vibrational modes in molecules, fluorescence is a powerful tool [26], while light emission in metals is weaker than molecules due to strong electron–electron (e–e) interaction and electron–phonon (e–ph) coupling [27]. Barati et al. [28] reported efficient electron–hole (e–h) pair generation in the transition-metal dichalcogenides (TMDs) semiconductors at temperatures near $T = 300$ K, resulting in 350% enhancement in the optoelectronic responsively [28]. Zhang et al. [29] investigated the polariton dispersions and anticrossing mode in TMDs and reported the existence of polariton modes at room temperature analyzing the PL and reflectance spectrum experimentally. Experimental study by Chen et al. [30] revealed that the light–matter quasiparticles (QPs), as valley-polarized plasmon polaritons, emit polarized light in the embedded 2D $MoS_2$ semiconductor in a cavity. The dispersive phonon polariton modes have also been reported in the hexagonal boron nitride monolayer and its heterostructure with graphene, where mid-infrared (IR) optical properties can be observed due to phonon polariton modes [31].

In the current research, we first studied the stability and electronic properties of honeycomb SiB monolayers using first-principles calculations. Different surface functionalization configurations are considered to attain structural stability and to tailor the electronic properties of a functionalized SiB monolayer. Optical properties of SiB and semihydrogenated SiB (H-SiB) (the most stable functionalized structure) are then estimated. We computationally illustrated how to tune the bandgap and accordingly on the light absorption on the surface of the materials with strain engineering. Second, we employed a comprehensive quantum approach of light emission from SPP semiconductor to link the HC generation to light emission and open an avenue to the experimentalists how to use PL spectroscopy to harvest long-lived HC light emission and optimize the efficiency of SPP detectors. Our study describes how to apply external stimuli such as strain and temperature to enhance the luminescence from SP in low dimensional semiconductors considering both e–ph and e–e scattering and polarizability, as two main factors, to enhance the light emission. Importantly, our quantum computational approach quantitatively describes HC distribution as a feature in the HC generation process in both unstrained and strained 2D semiconductors.

# 2 Methods

Density functional theory (DFT) is used to study the effect of surface functionalization on the stability and electronic and optical properties of a honeycomb SiB monolayer and the effect of strain on its electronic and optical properties. Density functional perturbation theory [32], as implemented in QUANTUM ESPRESSO [33], Green's function and time-dependent DFT were employed to compute the excited states and effect of temperature on the photo illumination of H-SiB.

## 2.1 Electronic and optical properties calculations

The electronic properties of SiB and H-SiB and the optical properties of H-SiB were computed utilizing first-principles many-body perturbation theory (MBPT) BerkeleyGW (BGW) (BerkeleyGW, Oakland, CA, USA) [34–36] package with a Perdew, Burke, and Ernzerhof starting point. GW approach and Beth–Salpeter equation (BSE) are described in Sections S3 and S4 in SI, respectively.

### 2.2 Exciton–plasmon interaction in semiconductors

The main parameters in the calculation of exciton–plasmon interaction are noninteracting $\chi^0(q, \omega)$ and interacting $\chi(q, \omega)$ polarizability. The density–density response function of noninteracting electrons in the reciprocal space $[\chi^0_{GG'}(q, \omega)]$ and interacting polarizability $\chi_{GG'}$ are calculated to understand the exciton–plasmon interactions in H-SiB. The effect of temperature on the polarizability and self-energy is also studied. The details are given in SI (Sections S7–S10). We, then, calculated the diagonal elements of the random phase approximation dielectric function $\varepsilon_{GG'}$ (see Eq. S30). Then plasmon modes can be obtained when the real part of dielectric function $[\varepsilon(q, \omega)]$ is set to zero. The electron energy loss (EEL) function is considered as the imaginary part of the inverse of the dielectric function $\varepsilon(q, \omega)$.

### 2.3 Light emission

After calculating the scattering process (Section S11 in SI), we used Green's function and nonequilibrium BSE, taking into account the e–h interactions, to compute the light absorption and emission [37, 38]. The details are given in SI (Section S12).

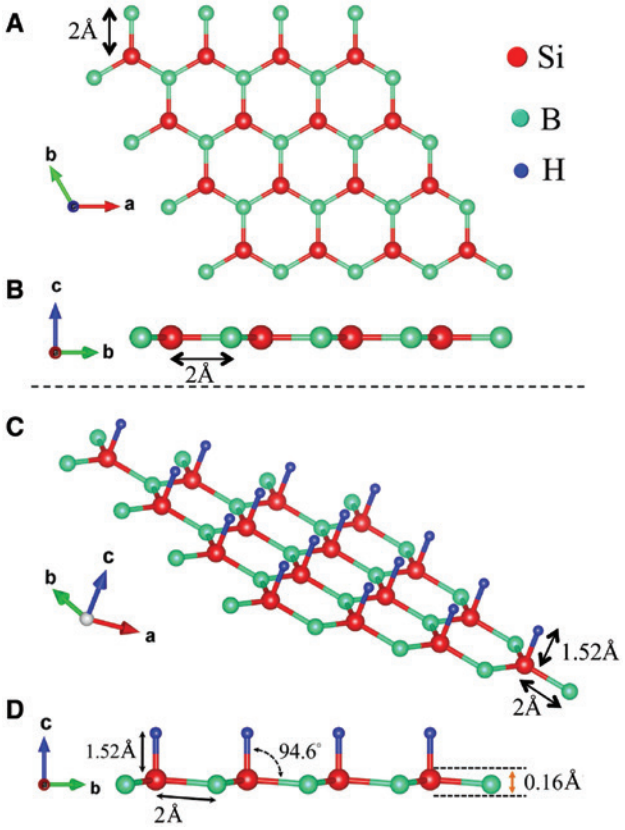


**Figure 1:** Crystallographic structure of SiB and H-SiB monolayers. (A) Top and (B) side views of pristine honeycomb SiB monolayer. (C) Top and (D) side views of the optimized structure of H-SiB monolayer. The hydrogen atoms are adsorbed onto the Si atomic sites. Red, cyan, and blue balls show silicon, boron, and hydrogen atoms, respectively.

## 3 Results and discussion

### 3.1 Dynamical stability

The graphene-like structure of a silicon boride monolayer is fully relaxed using the quasi-Newton method to determine the equilibrium atomic positions (Figure 1A, B) as this algorithm is very fast and efficient close to local minima. In this method, the atomic forces and the stress tensor are used to determine the equilibrium positions [33]. Also, the lattice constants of this unit cell are optimized using the Birch–Murnaghan equation state [39, 40] The results show that a pure SiB monolayer has a fully flat structure, and the optimized lattice constants, a = b = 3.4 Å, are in good agreement with previous results presented by Hansson et al. [8]. The phonon dispersion spectrum for pure SiB monolayer has a negative vibrational mode (Figure S1), establishing that it is dynamically unstable. To reach the goal of stabilizing the structure, surface functionalization using hydrogen atoms is here used in different configurations. The results show that semifunctionalized monolayers, for which the H atoms are adsorbed onto boron atoms, do not reach a stable form after force minimization calculations. Thus, semifunctionalization on silicon sites leads to stability, and we limit force minimization to these configurations (Figure 1C, D).

### 3.2 Electronic properties

The band diagrams of H-SiB monolayer are illustrated in Figure 2. Our results show that SiB monolayer is a nonmagnetic metal with partially occupied states around the Fermi level. As silicon and boron atoms have three $sp^2$ bonds in a honeycomb configuration, the σ bands are fully occupied and are located below the Fermi level. On the other hand, the $p_z$ orbitals of Si hybridize with $p_z$ orbitals of boron, and the hybridized π orbitals contribute symmetrically to both sides of the SiB monolayer. These π orbitals are partly filled and create a metallic band around the Fermi level (Figure 3A). As can be seen in this figure, pure SiB monolayer, the Fermi

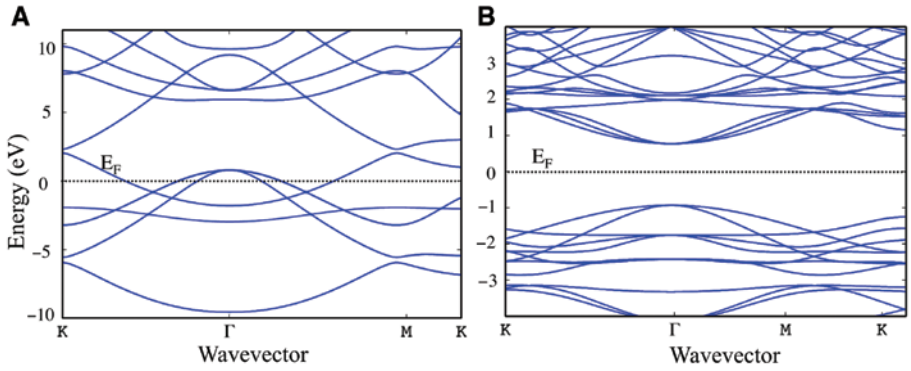


**Figure 2:** Calculated band structure with GW for pure SiB monolayer.
The band structure is plotted along the high symmetry k-path, K – Γ – M – K. The black dashed line denotes the Fermi level at zero energy.

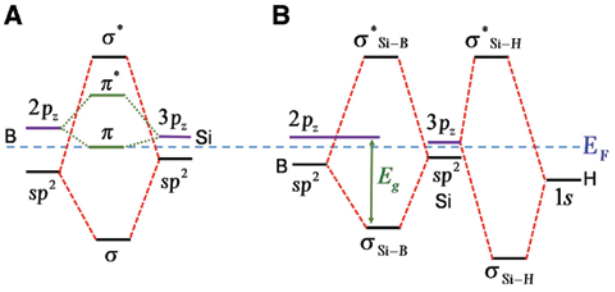


**Figure 3:** Band diagram for pure (A) and (B) semihydrogenated SiB.

level lies in the π band of the hybridized B-2$p_z$ and Si-3$p_z$ orbitals. So, when a hydrogen atom bonds with a Si atom, it just changes the 3$p_z$ configuration of Si atoms and forms a σ bond between hydrogen and Si-3$p_z$ ($\sigma_{Si\text{-}H}$). As a result, the empty 2$p_z$ orbitals of boron do not hybridize with Si-3$p_z$ and locate above the Fermi level. Finally, this mechanism leads to creation of an energy gap between bonding $\sigma_{Si\text{-}B}$ and non-bonding 2$p_z$ bands (Figure 3B).

Partial density of states (PDOS) calculations indicates that σ ($p_x + p_y$) and π ($p_z$) bands are fully and partly filled, respectively, for a pure SiB monolayer. Figure 4A and C exhibit the PDOS of $p_z$ and $p_x + p_y$ orbitals, of silicon and boron atoms in the pure SiB monolayer, respectively. Both bonding $p_x + p_y$ orbitals are fully occupied, while the $p_z$ orbitals cross the Fermi level. The PDOS for silicon and boron atoms in H-SiB (Figure 4B, D) confirms our inferred band diagram of H-SiB structure. Therefore, the SiB monolayer experiences a transition from metal to semiconductor after semihydrogenation.

## 3.3 Strain engineering the electronic and optical properties

The unstrained H-SiB monolayer is a direct semiconductor along the Γ direction and remains of direct type under strains in the range −6% to +6%, where the negative strain is compressive and the positive is tensile (Figure 5A–G).

The energy gap region is highlighted in yellow for all cases. Figure 5A–G show that H-SiB experiences a bandgap reduction under compressive strain and an expansion under tensile strain. We developed an empirical equation to correlate the bandgap energy of the material to the applied external strain (Figure 5H):

$$E_g = 0.07\,\varepsilon + 2.25 \tag{1}$$

where $E_g$ is the bandgap energy, and $\varepsilon$ is the applied external strain. As can be seen in Figure 5H, this relationship is linear. As the behavior of the material in the domain of applied strain (−6% to +6%), is linear (Figure S2), the gap energy of the material increases linearly when the applied external increases from −6% to +6% (Figure 5).

Optical properties of unstrained and strained H-SiB were computed based on first-principles MBPT as implemented in BGW (see Methods). We compared the optical properties of H-SiB monolayer without considering e–h interactions and with e–h (excitonic) interactions using BSE. Previous studies revealed that excitonic effects modify the optical properties of bulk [41, 42] and nanopore Si [43] and even more enhance the exciton binding energy of Si nanowires [44, 45].

Both real [$\epsilon_1(\omega)$] and the imaginary [$\epsilon_2(\omega)$] parts of the dielectric function are calculated using BGW and demonstrated in Figure 6. In Figure 6, the imaginary and real parts of dielectric function and absorption and reflectivity of SiB and H-SiB with and without e–h (exciton) interactions are indicated. Strong interactions of particle–antiparticle (e–h) result in pair excitonic effects, which drastically affect the photoresponse of nanoscale devices. These graphs confirm that considering the e–h interactions enhances optical absorption spectrum in visible range.

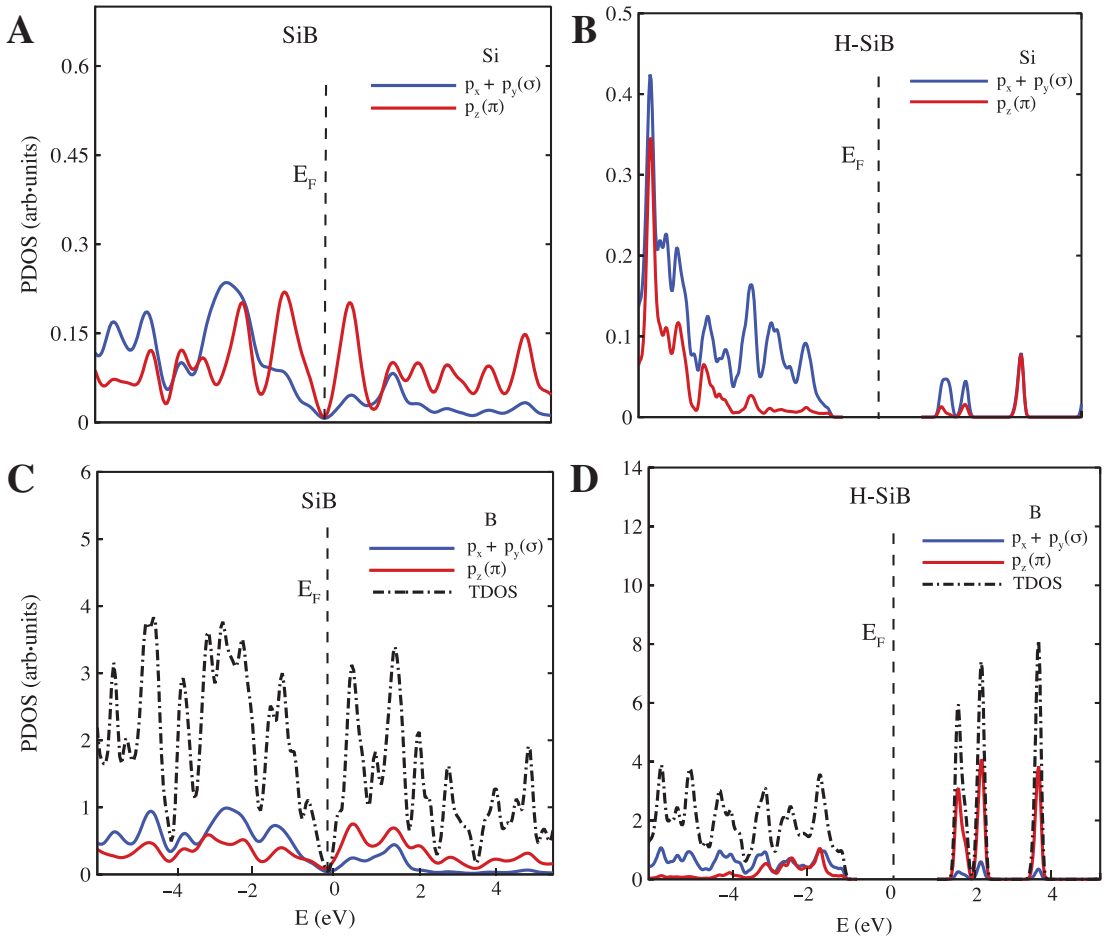


**Figure 4:** Total density of states for (A) pure and (B) semihydrogenated SiB monolayer and partial density of states of $p_z$ and $p_x + p_y$ suborbitals for silicon and boron atoms in (C) pure and (D) semihydrogenated SiB monolayer.

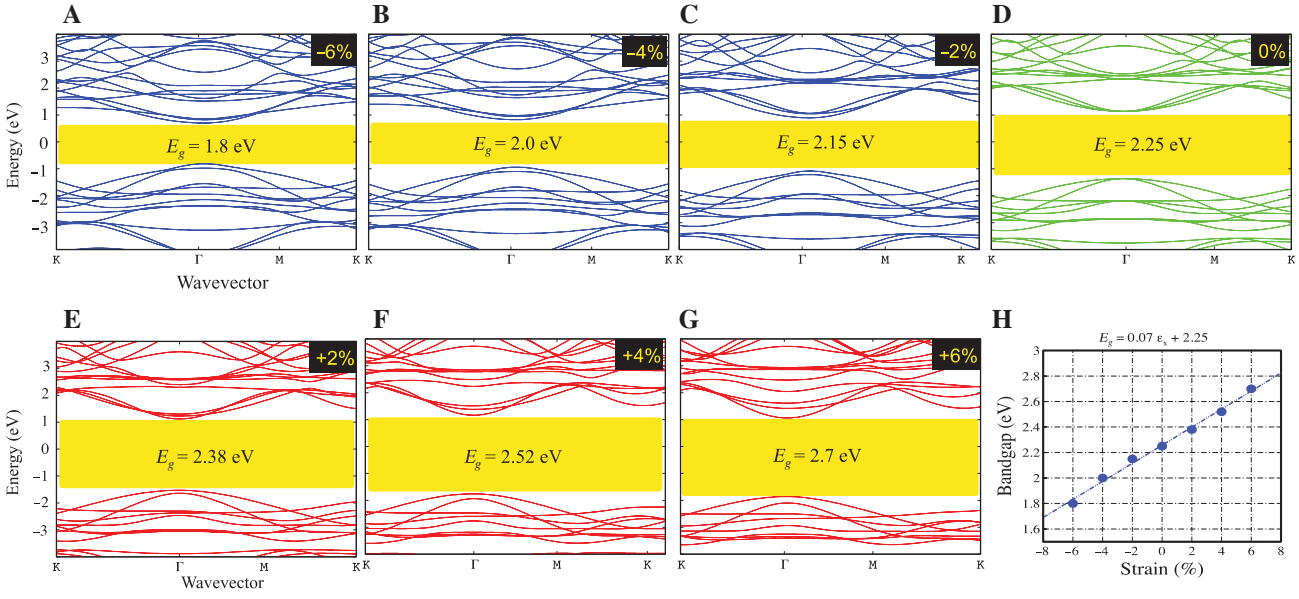


**Figure 5:** Electronic band structure of unstrained and strained H-SiB under strain ranging from −6% to 6%.
The gap direction remains direct, Γ to Γ, over the whole of applied strain range, −6% to +6%. The gap region is highlighted in yellow.

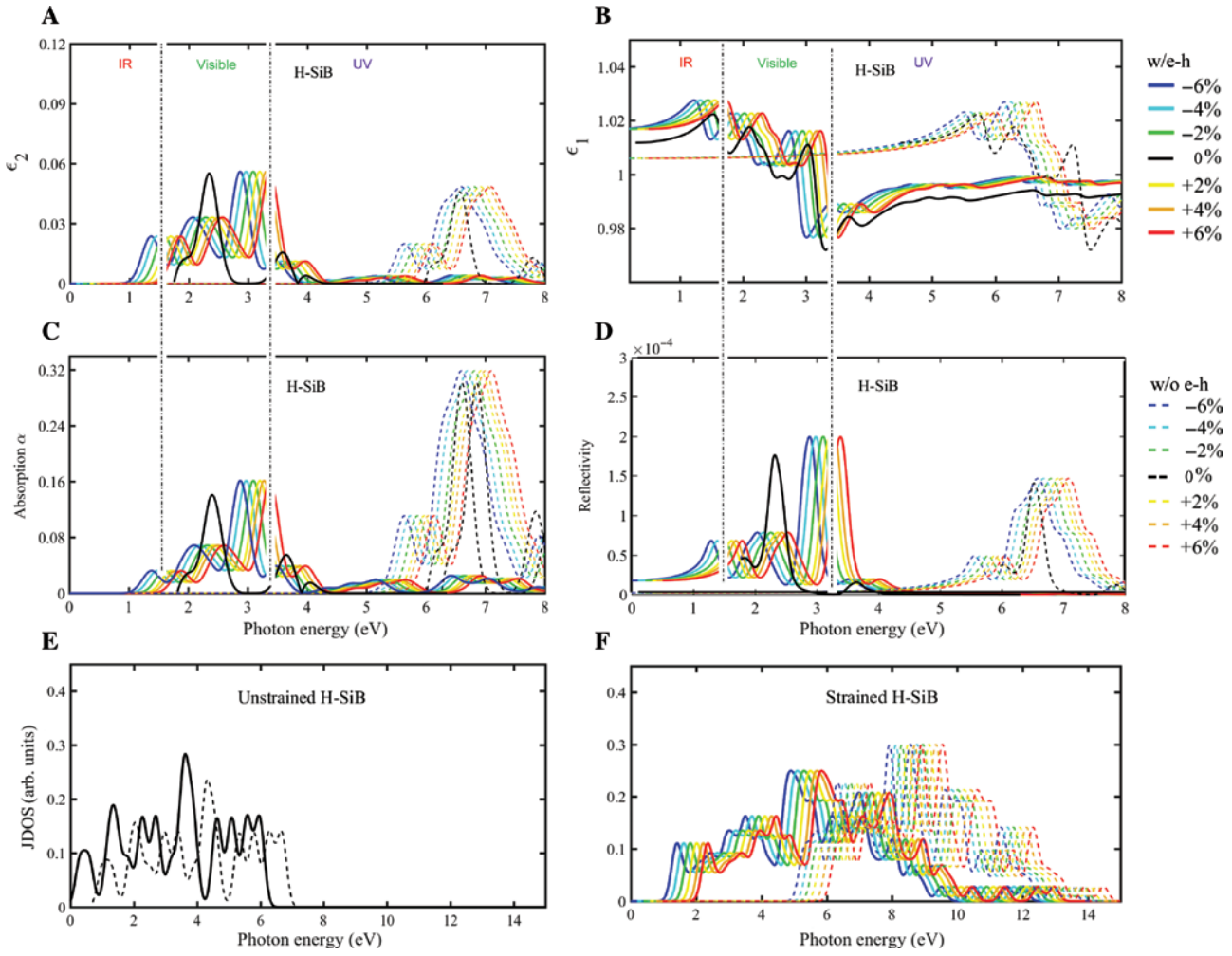


**Figure 6:** (A) Imaginary ($\epsilon_2$) and (B) real part ($\epsilon_1$) of dielectric function of unstrained and strained H-SiB. (C) Absorption ($\alpha$) and (D) Reflectivity coefficients of unstrained and strained H-SiB with and without electron–hole (e–h) interaction. Joint density of states (JDOS) of (E) unstrained and (F) strained H-SiB with (solid lines) and without (dashed lines) e–h (exciton) interactions.

The strain field modifies the absorption spectra (Figure 6C) and the optical gap of the H-SiB monolayer, both of which are crucial physical quantity for the device operation. As displayed in Figure 6C, compressive strains shift the absorption spectrum to a lower energy (red shift), whereas tensile strains shift the absorption spectrum to an upper energy (blue shift). The compressive strain deforms covalent bonds toward reduction of screening effect; therefore, the photoexcited QP in the H-SiB monolayer experiences stronger Coulomb interactions. Consequently, the compressive strained H-SiB emitted lower photon energy in comparison to the tensile strained nanostructures.

## 3.4 Surface plasmons

Surface plasmons (SPs) are collective longitudinal oscillations of valence electrons in metals or semiconductors that enable control of electromagnetic energy and confinement at subwavelength scale [46]. In general, SPs can exist in any material with mobile charge carriers, which show reactive response to the electric field [46]. The EEL spectroscopy is a main tool for detecting collective excited electrons due to SPs. Figure 7 shows the EEL function for different momentum transfer vectors, **q** in unstrained and strained H-SiB monolayers with and without considering e–h interactions. This figure suggests that SP exists and shows a blue shift for different momentum transfer vectors as a result of interband transition. Due to the structural deformation in the strained H-SiB monolayers, their EEL function shows three peaks, which confirms the strong inelastic scattering in the strained nanostructures. To compare the dispersion of SP for unstrained and strained H-SiB, we calculated [$\omega$ ($q$)] as a dispersion function, obtained by GW calculations, as can be seen in Figure 8. Importantly, the dispersion modes of SP improve for strained H-SiB, supporting previous EEL results.

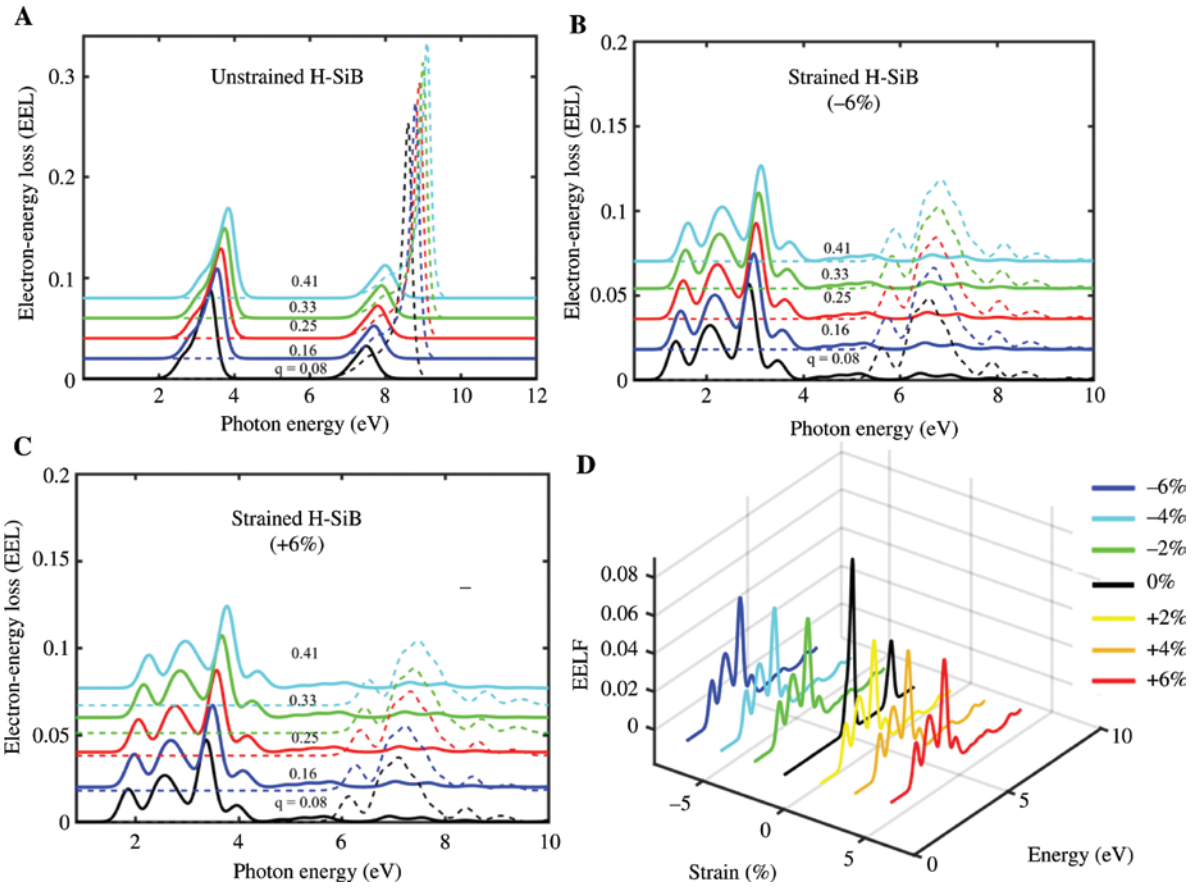


**Figure 7:** Electron-energy loss (EEL) function for different momentum transfers; for (A) unstrained, (B) 6% compressive strained, and (C) 6% tensile strained H-SiB with/without e–h interactions; (D) 3D plot of EEL as a function of strain and photon energy.

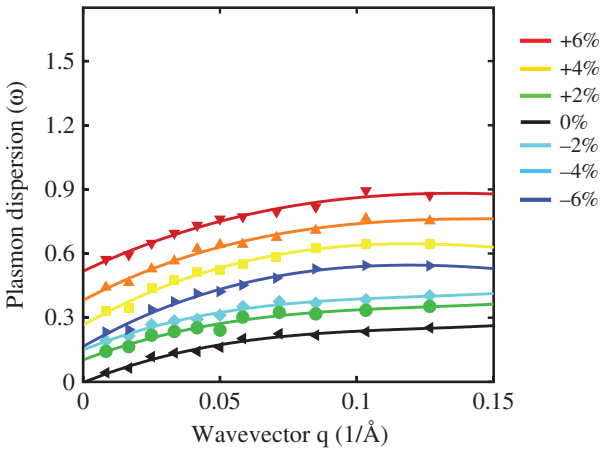


**Figure 8:** Plasmon modes dispersion [$\omega$ ($q$)] for unstrained and strained H-SiB.

## 3.5 Light emission

Surface plasmons enhance photoluminescence in metal nanomaterials [27]. To apply this concept for 2D semiconductors and acquire all light spectral features of H-SiB monolayers including thermal parameters on the light emission, we further compute the polarizability matrix. The polarizability of H-SiB monolayer is reported in Figure 9A. Strain (displacement of atoms) and polarization are correlated due to the fact that applying strain on dielectric crystal creates a net dipole moment, which induces additional polarization to the system [47]. Therefore, strained structures possess larger polarizability. Accordingly, in the current research, the strained H-SiB structures show larger polarizability than unstrained H-SiB (Figure 9A). Figure 9B and D present the temperature evolution of polarizability in both unstrained and strained structures. As can be seen in Figure 9, the polarization of H-SiB monolayers decreases with increasing the temperature, which can be correlated to the screening properties of 2D materials. We note that the screening effect of 2D materials increases by temperature due to increasing the scattering rate. The temperature polarizability function $\chi(q)$ is defined from the dielectric screening function $\epsilon(q)$ as follows: $\epsilon(q) = 1 + v(q)\chi(q)$, where $v(q)$ is the 2D screening Coulomb interaction, and $\chi(q) = g_s g_v \sum_k \frac{f(\varepsilon_k) - f(\varepsilon_{|k+q|})}{\varepsilon_k - \varepsilon_{|k+q|}}$,

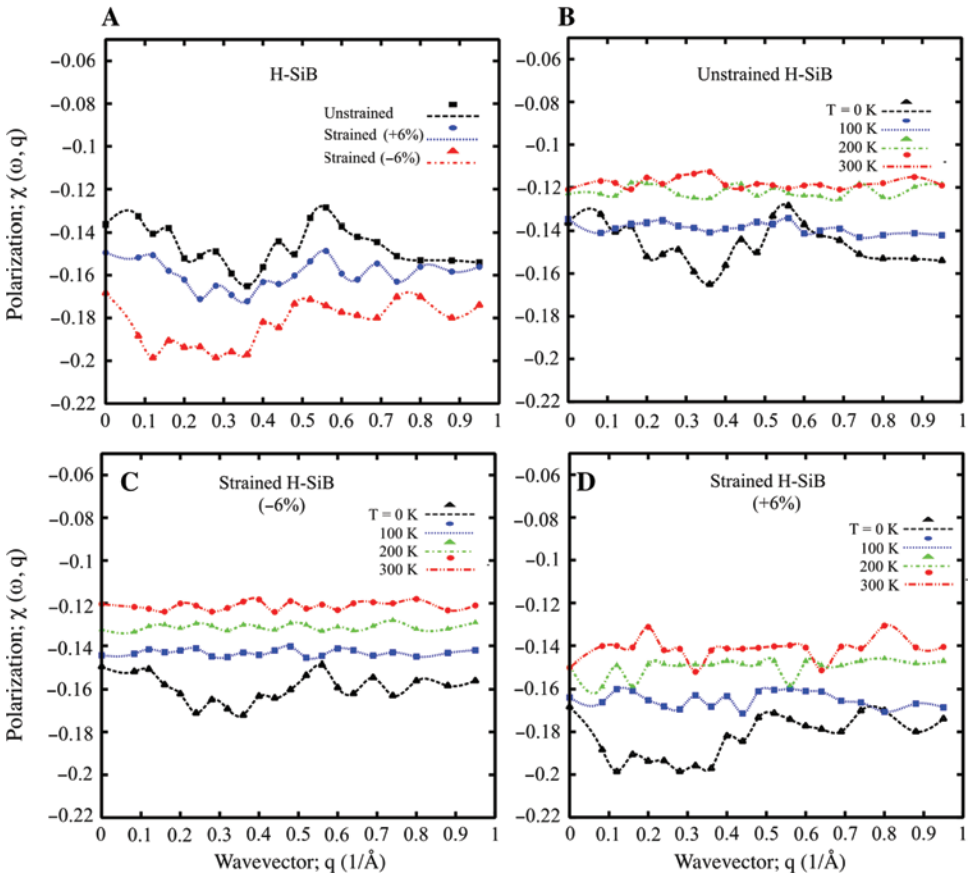


**Figure 9:** Dipole matrix elements or polarization $\chi(\omega, q)$ for unstrained and strained H-SiB (A–D).

where $f(\varepsilon_k)$ is the Fermi distribution function [48]. This picture can be linked to the temperature dependency of H-SiB polarizability.

As HCs in semiconductors are created due to strain and temperature, we calculated the luminescence spectra at finite temperatures and in the presence and absence of strain to understand the effect of HCs on the light emission in H-SiB (Figures 10 and 11). We used Eqs. S42–S44 to compute the phonon assisted luminescence spectrum (Figure 10). All spectra showed a red shift with increasing temperature. This resulted from the enhanced inelastic scattering (loss of energy) as discussed in the previous section and strong e–ph coupling and interaction during the temperature increase. Zhang et al. [49] experimentally reported temperature-dependent photoluminescence of strained and unstrained GaSe nanosheets and found that red shift happened. In Figure 10A, there are two main peaks at 1.13 and 5.16 eV, which can be seen for the unstrained structure. The main peak is shifted from 1.13 eV to 0.74, 0.62, and 0.53 eV, respectively, when the temperature increased from 0 K to 100, 200, and 300 K (Figure 10A). In detail, Figure 11B highlights that the main peaks (peaks I, II) of unstrained H-SiB move toward invisible light region (IR) by increasing temperature. As discussed earlier in Figure 9B, the carrier energy for unstrained nanostructure decreases with increasing temperature. Therefore, the emitted light placed in the IR region has lower energy in comparison to the visible region. In Figure 10B and C, two main peaks at 2.19 and 3.07 eV are for the structure under 6% compressive, and 2.94 and 3.82 are for the structure under 6% tensile strain, respectively. The luminescence spectrum of the strained H-SiB structures under 6% compression deformation follows a similar pattern of unstrained structure, while here a red shift from 3.07 eV to 2.9, 2.81, and 2.64 eV can be, respectively, seen for the main peaks (peak III) when the temperature increases from 0 K to 100, 200, and 300 K (Figure 11C). For the tensile structure at 6% deformation, the same pattern can be observed in Figure 11C, where the main peak (peak III) is red shifted from 3.82 eV to 3.67, 3.54, and 3.38 eV (Figure 11C). A good explanation for the temperature effect on photoluminescence spectrum of strained structures can be attributed to decrease in polarizability of these structures with temperature (Figure 9C, D). Therefore, by increasing the

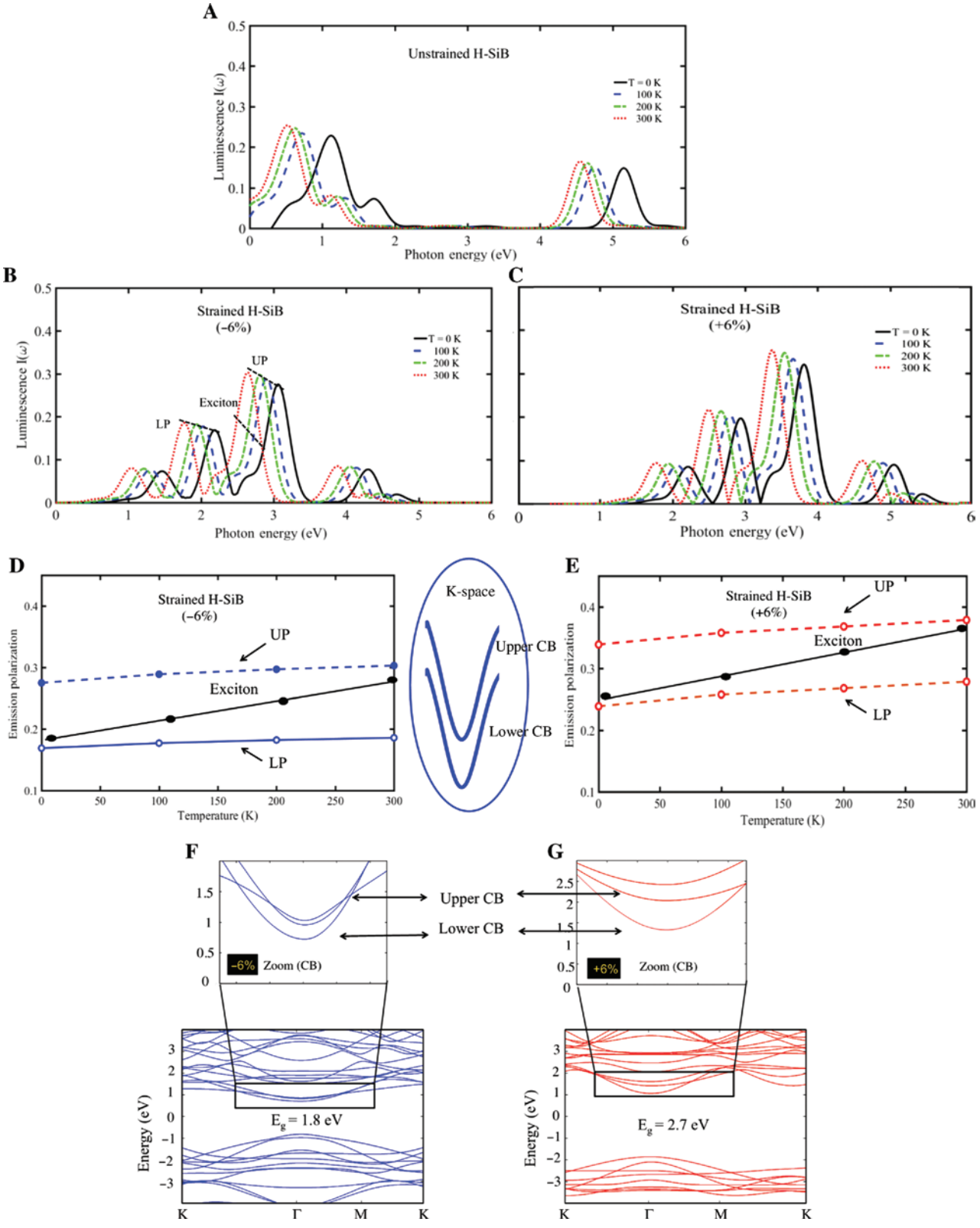


**Figure 10:** (A–C) Luminescence spectra for unstrained and strained H-SiB by considering electron–electron (e–e) and electron–phonon (e–ph) interaction. (D, E) Temperature-dependent valley-polarized exciton–polariton emission of upper polariton (UP) and lower polariton (LP) quasiparticle eigenstates in the strained H-SiB. The band structure with zooming in on the conduction band (CB) of (F) compressive strained (–6%) and (G) tensile strained (+6%) H-SiB.

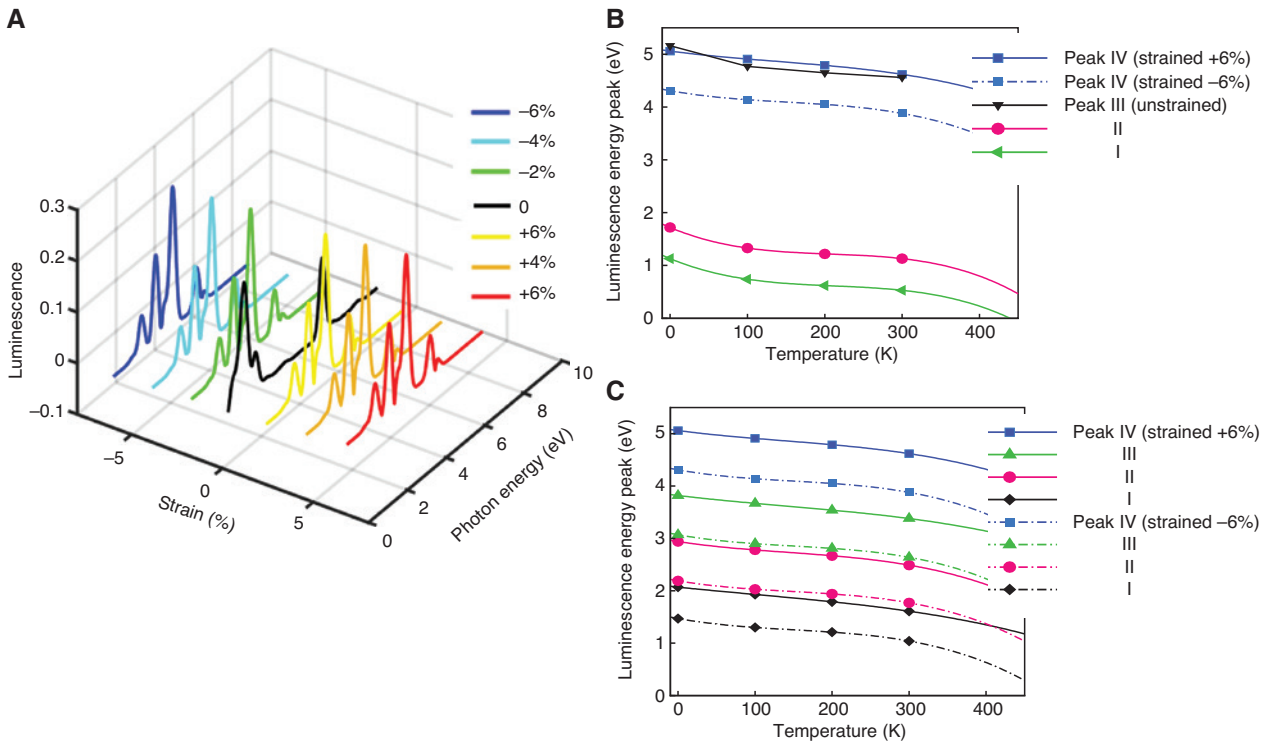


**Figure 11:** (A) Three-dimensional plot of luminescence function vs. strain and photon energy. Temperature-dependent of luminescence of peaks I, II, and III in (B) unstrained and (C) strained H-SiB. Solid and dashed lines are representatives of compressive (−6%) and tensile strain (6%), respectively.

temperature, the carrier energy decreases, and red shift (low energy) happens in the photoluminescence spectrum. To better understand the contributions of the mechanisms responsible for thermal effect, we considered a steady-state solution for the temperature-dependent intensity I for the exciton recombination, which is given by Eq. 2:

$$I = I_0[1 + a\ ex(-E_A / kT)]^{-1} \tag{2}$$

where $E_A$ is the thermal activation energy [50]. The application of temperature can lead to a change in activation energy with increasing the potential depth.

Cai et al. [27] showed an enhancement in the photoluminescence of gold nanoparticle due to the generation of HCs. Here, we note that HCs improve interlayer e–h interaction in the 2D semiconductors. Figure 10B and C support the idea that HC exciton created by SPP enhances the luminescence intensity (photon density of states) arising from thermal exciton and thermal SP. Figure 10D and E indicate the temperature-dependent valley-polarized exciton–polariton emission of upper polariton and lower polariton QP eigenstates in the strained (−6% and +6%) H-SiB monolayer. The exciton energies are calculated by GW approach and BSE [see SI (Sections S3, and S4) for more details]. The temperature- and strain-dependent photoluminescence suggests that we can tune the light emission in the visible light range for photoelectronic devices made of 2D semiconductors.

## 3.6 Decay rate and HC generation

To study SPP–electron coupling in the semiconductors, we developed a framework of perturbation theory and Feynman diagram for 2D semiconductors [see more computation details in the SI (Section S13)]. Figure 12A presents a schematic illumination of H-SiB monolayer, in which SPs are polarized and generate SPPs. Scattering of collective electrons of generated SPPs leads to their decay and results in the creation of excitons (pair of hot electron and hole). Figure 12B–D represent the hot hole and electron distribution for unstrained and strained H-SiB at different temperatures within windows of −4… 4 eV Fermi energy. Figure 12 reveals that at finite temperatures the scattering and decay rates of collective electrons of SPPs in H-SiB become more significant at distances far away Fermi level, which results in the generation of hot electrons and holes in those distances.

Figure 13 shows mean free path (MFP) of HCs in both unstrained and strained H-SiB monolayers at ground

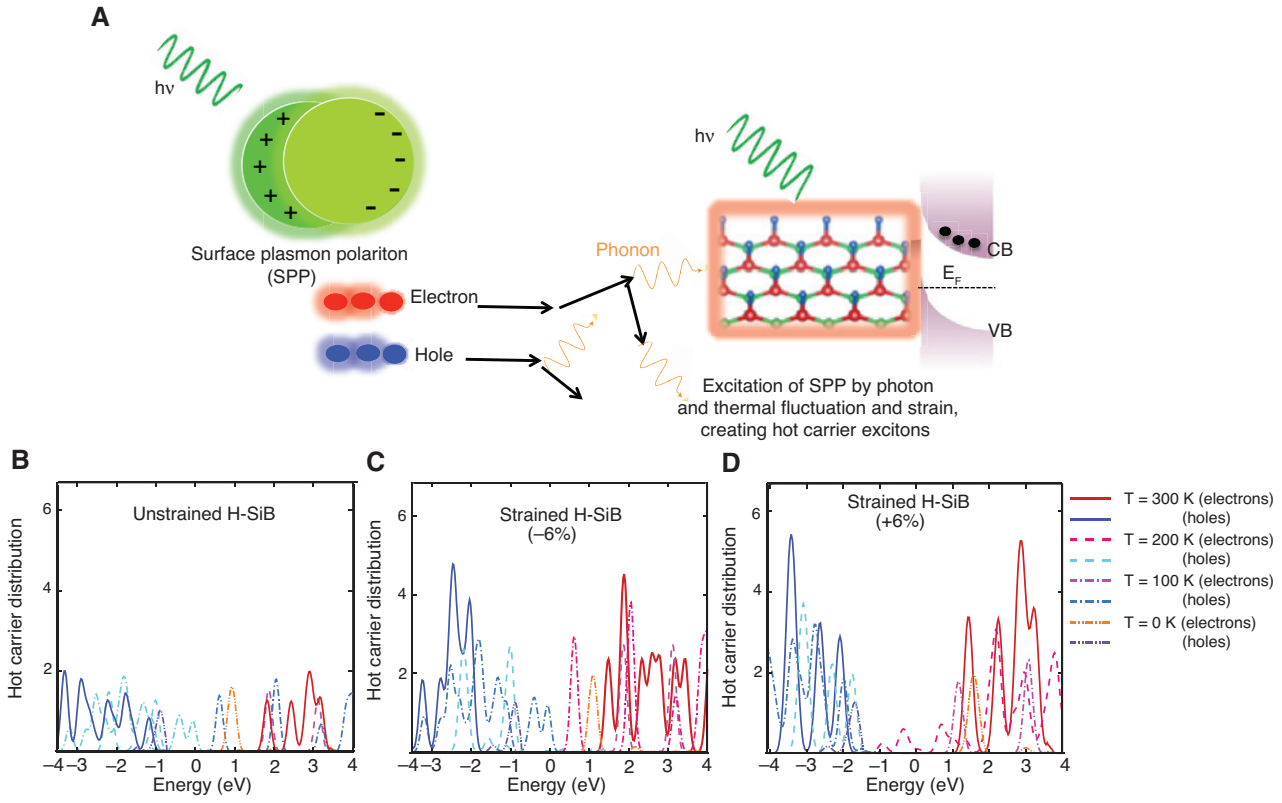


**Figure 12:** (A) Schematic of an H-SiB semiconductor under illumination, showing a polarization of SP and excited SPP and the decay of an SPP to an exciton (pair of hot electron and hole. (B) The HC distribution (red color represents electron, and blue color represents hole) of unstrained and strained H-SiB at different temperatures.

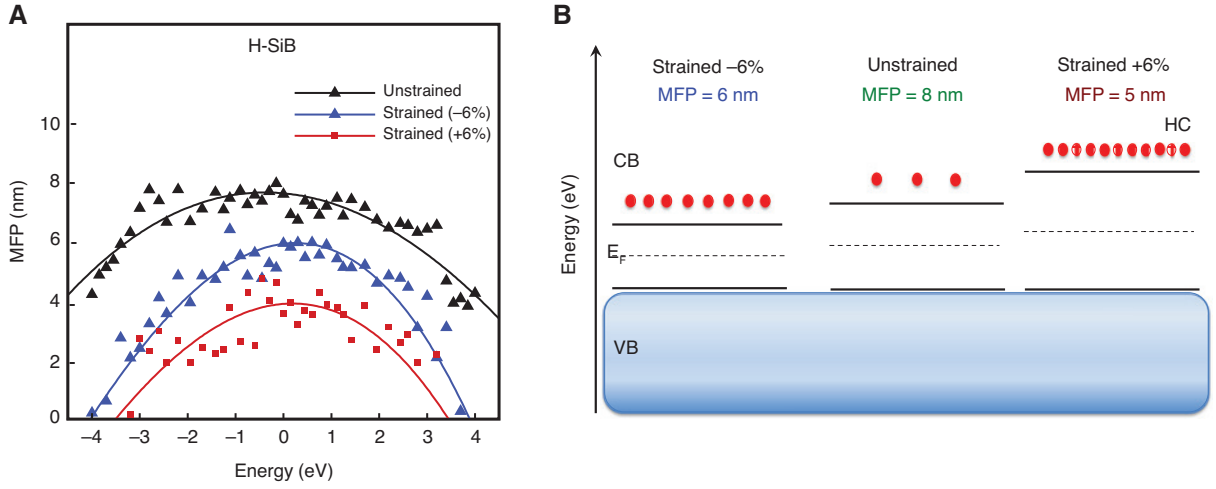


**Figure 13:** (A) The mean free path (MFP) of HCs and (B) mechanism of HC generation in unstrained and strained H-SiB. Red points are representatives of HCs.

state. To compute MFPs, the HC velocity (the slope of GW band structure) is multiplied into the total relaxation times of different temperatures [51]. Our results show a large spread of MFPs near the Fermi energy (Figure 13A). The total MFP for unstrained 6% compressive strained and 6% tensile strained structures is obtained as 8, 6, and 5 nm, respectively. By increasing the number of generated HCs in the structure, their MFP decreases. Here, as the maximum HCs are generated in the 6% tensile strained structure, the MFP of HCs is the shortest distance in comparison to

the other two structures (unstrained and 6% compressive strained). Additionally, a comparison of our calculated HC-MFP for 2D semiconductors (H-SiB) with the reported HC-MFP for metals (Au and Ag) [51] shows that MFPs in metals can range in the order 10 to 40 nm [51], while MFPs in H-SiB is in the order of 3 to 8 nm (Figure 13A). As can be seen in this figure, the MFP for unstrained H-SiB is the most significant one in comparison to both strained structures.

With regard to HC generation and its MFP at ground state, it should be noticed that polarizability of both strained H-SiB is greater than unstrained as discussed in Section 3.5 and Figure 9. This polarizability creates a built-in electric field in the system, which affects the carrier energy with ascending rate in the strained nanostructures. Therefore, the scattering rate of SPP on the strained H-SiB nanostructures enhances, which leads to the generation of a larger amount of HCs with smaller MFPs in comparison to the unstrained structures as shown in Figure 13.

As we only have the band structure for ground state, we have calculated only the MFP for the ground state. However, we believe that we will have the similar behavior at finite temperatures (at any finite temperature, unstrained and 6% tensile strained structure will have the maximum and minimum HC-MFP, respectively). Additionally, by increasing temperature, the mobility and scattering rate of carriers increase. This makes them lose their collective behavior. Then, the rate of MFPs for generated HC decreases with increasing temperature. Therefore, we expect to have the minimum HC-MFP for the 6% tensile strained structure at 300 K.

## 4 Conclusions

We use theory and computation to present a physical picture of SP valley polariton for 2D semiconductors using quantum mechanics. We developed a theoretical framework using MBPT and Feynman diagram to show how to generate HCs in low dimensional semiconductors by coupling exciton–SPPs. Our findings of the luminescence spectrum revealed that the light emission was improved with increasing strain and temperature due to the fact that the e–ph interactions are enhanced with increasing both strain and temperature. Applying strain and increasing temperature make a red shift occur in the luminescence spectrum. More importantly, we showed that SPPs in 2D semiconductors can be tuned by external stimuli parameters such as thermal excitation of charge carriers (pair of hot hole and electron) and generation of HCs. When the H-SiB monolayers projected under illumination, SPs are polarized, and SPPs are created. Excited SPPs by external stimuli (temperature and strain) decay and create excitons (e–h interactions). The scattering of these excitons causes the generation of HCs. The generated HCs are scattered and become stable by losing their energy through phonon emission process. Our research opens an avenue for the experimentalists to design 2D materials with high photovoltaic conversion efficiency and robust optical properties due to exciton–SPP coupling and HC generation for photocurrent, plasmonic photovoltaic, and optoelectronic nanodevices with high efficiency.

**Competing financial interest:** The authors declare no competing financial interest.

## References

[1] Novoselov KS, Geim AK, Morozov SV, et al. Electric field effect in atomically thin carbon films. Science 2004;306:666–9.
[2] Novoselov KS, Geim AK, Morozov SV, et al. Two-dimensional gas of massless Dirac fermions in graphene. Nature 2005;438:197–200.
[3] Tománek D, Wentzcovitch RM, Louie SG, Cohen ML. Calculation of electronic and structural properties of BC 3. Phys Rev B 1998;37:3134–6.
[4] Polyakov SN, Denisov VN, Mavrin BN, et al. Formation of boron-carbon nanosheets and bilayers in boron-doped diamond: origin of metallicity and superconductivity. Nanoscale Res Lett 2016;11:1–9.
[5] Li S-S, Zhang C-W, Ji W-X, Li F, Wang P-J. Tunable electronic properties induced by a defect-substrate in graphene/$BC_3$ heterobilayers. Phys Chem Chem Phys 2014;16:22861–6.
[6] Xu L, Dai Z, Sui P, Sun Y, Wang W. Electronic properties of fluorinated/semi-fluorinated boron–carbon monolayer: a first-principles study. Comp Mater Sci 2015;99:343–7.
[7] Hussain T, Searles DJ, Takahashi K. Reversible hydrogen up take by BN and $BC_3$ monolayers functionalized with small Fe clusters: a route to effective energy storage. J Phys Chem A 2016;120:2009–13.
[8] Hansson A, Mota FDB, Rivelino R. Unusual electronic properties and transmission in hexagonal SiB monolayers. Phys Chem Chem Phys 2014;16:14473–8.
[9] Şahin H, Cahangirov S, Topsakal M, et al. Monolayer honeycomb structures of group-IV elements and III–V binary compounds: first-principles calculations. Phys Rev B 2009;80:155453.
[10] Adamska L, Sadasivam S, Foley IV JJ, Darancet P, Sharifzadeh S. First-principles investigation of borophene as a monolayer transparent conductor. J Phys Chem C 2018;122:4037–45.
[11] Adamska L, Sharifzadeh S. Fine-tuning the optoelectronic properties of freestanding borophene by strain. ACS Omega 2017;2:8290–9.
[12] Dai J, Zhao Y, Wu X, Yang J, Zeng XC. Exploration of structures of two-dimensional boron–silicon compounds with $sp_2$ silicon. J Phys Chem Lett 2013;4:561–7.

[13] Ding Y, Wang Y. Density functional theory study of the silicene-like SiX and XSi3 (X=B, C, N, Al, P) honeycomb lattices: the various buckled structures and versatile electronic properties. J Phys Chem C 2013;117:18266–78.
[14] Aizawa T, Suehara S, Otani S. Two-dimensional silicon boride on ZrB2(0001). Phys Rev Mater 2019;3:014005.
[15] Low T, Chaves A, Caldwell JD, et al. Polaritons in layered two-dimensional materials. Nat Mat 2017;16:182–94.
[16] Mubeen S, Lee J, Singh N, Kramer S, Stucky GD, Moskovits M. An autonomous photosynthetic device in which all charge carriers derive from surface plasmons. Nat Nanotechnol 2013;8:247–51.
[17] Zheng BY, Zhao H, Manjavacas A, McClain M, Nordlander P, Halas NJ. Distinguishing between plasmon-induced and photoexcited carriers in a device geometry. Nat Commun 2015;6:7797.
[18] Sheldon MT, van de Groep J, Brown AM, Polman A, Atwater HA. Plasmoelectric potentials in metal nanostructures. Science 2014;346:828–31.
[19] Marimuthu A, Zhang J, Linic S. Tuning selectivity in propylene epoxidation by plasmon mediated photo-switching of Cu oxidation state. Science 2013;339:1590–3.
[20] Brandt NC, Keller EL, Frontiera RR. Ultrafast surface-enhanced raman probing of the role of hot electrons in plasmon-driven chemistry. J Phys Chem Lett 2016;7:3179–85.
[21] Knight MW, Sobhani H, Nordlander P, Halas NJ. Photodetection with active optical antennas. Science 2011;332:702–4.
[22] Naik GV, Welch AJ, Briggs JA, Solomon ML, Dionne JA. Hot-carrier–mediated photon upconversion in metal-decorated quantum wells. Nano Lett 2017;17:4583–7.
[23] Brongersma ML, Halas NJ, Nordlander P. Plasmon-induced hot carrier science and technology. Nat Nanotechnol 2015;10:25–34.
[24] Pfeiffer W, Kennerknecht C, Merschdorf M. Electron dynamics in supported metal nanoparticles: relaxation and charge transfer studied by time-resolved photoemission. Appl Phys A Mater Sci Proc 2004;78:1011–28.
[25] Harutyunyan H, Martinson AB, Rosenmann D, et al. Anomalous ultrafast dynamics of hot plasmonic electrons in nanostructures with hot spots. Nat Nanotechnol 2015;10:770–4.
[26] Hsu CP, Georgievskii Y, Marcus RA. Time-dependent fluorescence spectra of large molecules in polar solvents. J Phys Chem A 1998;102:2658–66.
[27] Cai Y, Liu JG, Tauzin LJ, et al. Photoluminescence of gold nanorods: Purcell effect enhanced emission from hot carriers. ACS Nano 2018;122:976–85.
[28] Barati F, Grossnickle M, Su S, Lake RK, Aji V, Gabor NM. Hot carrier–enhanced interlayer electron–hole pair multiplication in 2D semiconductor heterostructure photocells. Nat Nanotech 2017;12:1134–9.
[29] Zhang L, Gogna R, Burg W, Tutuc E, Deng H. Photonic-crystal exciton-polaritons in monolayer semiconductors. Nat Commun 2018;9:713.
[30] Chen YJ, Cain JD, Stanev TK, Dravid VP, Stern NP. Valley-polarized exciton–polaritons in a monolayer semiconductor. Nat Photonics 2017;11:431–5.
[31] Kumar A, Low T, Fung KH, Avouris P, Fang NX. Tunable light–matter interaction and the role of hyperbolicity in graphene–hBN system. Nano Lett 2015;15:3172–80.
[32] Gonze X, Lee C. Dynamical matrices, Born effective charges, dielectric permittivity tensors, and interatomic force constants from density-functional perturbation theory. Phys Rev B 1997;55:10355–68.
[33] Giannozzi P, Baroni S, Bonini N, et al. QUANTUM ESPRESSO: a modular and open-source software project for quantum simulations of materials. J Phys Condens Matter 2009;21:395502.
[34] Hybertsen MS, Louie SG. Electron correlation in semiconductors and insulators: band gaps and quasiparticle energies. Phys Rev B Condens Matter 1986;34:5390–413.
[35] Rohlfing M, Louie SG. Electron–hole excitations and optical spectra from first principles. Phys Rev B 2000;62:4927.
[36] Deslippe J, Samsonidze G, Strubbe DA, et al. A massively parallel computer package for the calculation of the quasiparticle and optical properties of materials and nanostructures. Comput Phys Commun 2012;183:1269–89.
[37] Martin RM, Reining L, Ceperley DM. Interacting electrons. Cambridge, United Kingdom: Cambridge University Press, 2016.
[38] Strinati G. Application of the Green's functions method to the study of the optical properties of semiconductors. Riv Nuovo Cimento 1988;11:1–86.
[39] Birch F. Finite elastic strain of cubic crystals. Phys Rev 1947;71:809–24.
[40] Murnaghan FD. The compressibility of media under extreme pressures. Proc Natl Acad Sci USA 1944;30:244–7.
[41] Albrecht S, Reining L, Del Sole R, Onida G. Ab initio calculation of excitonic effects in the optical spectra of semiconductors. Phys Rev Lett 1998;80:4510–13.
[42] Rohlfing M, Louie SG. Electron–hole excitations and optical spectra from first principles. Phys Rev B 2000;62:4927–44.
[43] Shi G, Kioupakis E. Electronic and optical properties of nanoporous silicon for solar-cell applications. ACS Photonics 2015;2:208–15.
[44] Yang L, Spataru CD, Louie SG, Chou MY. Enhanced electron–hole interaction and optical absorption in a silicon nanowire. Phys Rev B 2007;75:201304.
[45] Bruno M, Palummo M, Marini A, Del Sole R, Ossicini S. From Si nanowires to porous silicon: the role of excitonic effects. Phys Rev Lett 2007;98:036807.
[46] Fei Z, Rodin AS, Andreev GO, et al. Gate-tuning of graphene plasmons revealed by infrared nano-imaging. Nature 2012;487:82.
[47] Maranganti R, Sharma P. Atomistic determination of flexoelectric properties of crystalline dielectrics. Phys Rev B 2009;80:054109.
[48] Sarma SD, Hwang EH. Screening and transport in 2D semiconductor systems at low temperatures. Sci Rep 2015;5:16655.
[49] Zhang D, Jia T, Dong R, Chen D. Temperature-dependent photoluminescence emission from unstrained and strained gase nanosheets. Materials 2017;10:1282.
[50] Luo Y, Liu N, Hone JC, Strauf S. Single photon emission in $WSe_2$ up 160 K by quantum yield control. 2D Mater 2019;6:035017.
[51] Bernardi M, Mustafa J, Neaton JB, Louie SG. Theory and computation of hot carriers generated by surface plasmon polaritons in noble metals. Nat Commun 2015;6:7044.

**Supplementary Material:** The online version of this article offers supplementary material (https://doi.org/10.1515/nanoph-2019-0363).